

# DENSE MOLECULAR GAS EXCITATION IN NUCLEAR STARBURSTS AT HIGH REDSHIFT: HCN, HNC, AND HCO<sup>+</sup>( $J = 6 \rightarrow 5$ ) EMISSION IN THE $z = 3.91$ QUASAR HOST OF APM 08279+5255

DOMINIK A. RIECHERS<sup>1,6</sup>, AXEL WEISS<sup>2</sup>, FABIAN WALTER<sup>3</sup>, AND JEFF WAGG<sup>4,5</sup>

<sup>1</sup> Astronomy Department, California Institute of Technology, MC 249-17, 1200 East California Boulevard, Pasadena, CA 91125, USA; [dr@caltech.edu](mailto:dr@caltech.edu)

<sup>2</sup> Max-Planck-Institut für Radioastronomie, Auf dem Hügel 69, Bonn, D-53121, Germany

<sup>3</sup> Max-Planck-Institut für Astronomie, Königstuhl 17, Heidelberg, D-69117, Germany

<sup>4</sup> National Radio Astronomy Observatory, P.O. Box O, Socorro, NM 87801, USA

<sup>5</sup> European Southern Observatory, Alonso de Córdova 3107, Vitacura, Casilla 19001, Santiago 19, Chile

Received 2010 June 25; accepted 2010 October 8; published 2010 November 22

## ABSTRACT

We report the detection of surprisingly strong HCN( $J = 6 \rightarrow 5$ ), HNC( $J = 6 \rightarrow 5$ ), and HCO<sup>+</sup>( $J = 6 \rightarrow 5$ ) emission in the host galaxy of the  $z = 3.91$  quasar APM 08279+5255 through observations with the Combined Array for Research in Millimeter-wave Astronomy. HCN, HNC, and HCO<sup>+</sup> are typically used as star formation indicators, tracing dense molecular hydrogen gas [ $n(\text{H}_2) > 10^5 \text{ cm}^{-3}$ ] within star-forming molecular clouds. However, the strength of their respective line emission in the  $J = 6 \rightarrow 5$  transitions in APM 08279+5255 is extremely high, suggesting that they are excited by another mechanism besides collisions in the dense molecular gas phase alone. We derive  $J = 6 \rightarrow 5$  line luminosities of  $L'_{\text{HCN}} = (4.9 \pm 0.6)$ ,  $L'_{\text{HNC}} = (2.4 \pm 0.7)$ , and  $L'_{\text{HCO}^+} = (3.0 \pm 0.6) \times 10^{10} \mu_{\text{L}}^{-1} \text{ K km s}^{-1} \text{ pc}^2$  (where  $\mu_{\text{L}}$  is the lensing magnification factor), corresponding to  $L'$  ratios of  $\sim 0.23$ – $0.46$  relative to CO( $J = 1 \rightarrow 0$ ). Such high line ratios would be unusual even in the respective ground-state ( $J = 1 \rightarrow 0$ ) transitions, and indicate exceptional, collisionally and radiatively driven excitation conditions in the dense, star-forming molecular gas in APM 08279+5255. Through an expansion of our previous modeling of the HCN line excitation in this source, we show that the high rotational line fluxes are caused by substantial infrared pumping at moderate opacities in a  $\sim 220$  K warm gas and dust component. This implies that standard  $M_{\text{dense}}/L'$  conversion factors would substantially overpredict the dense molecular gas mass  $M_{\text{dense}}$ . We also find a HCN( $J = 6 \rightarrow 5$ )/HCN( $J = 5 \rightarrow 4$ )  $L'$  ratio greater than 1 ( $1.36 \pm 0.31$ )—however, our models show that the excitation is likely not “super-thermal,” but that the high line ratio is due to a rising optical depth between both transitions. These findings are consistent with the picture that the bulk of the gas and dust in this source is situated in a compact, nuclear starburst, where both the highly active galactic nucleus and star formation contribute to the heating.

**Key words:** cosmology: observations – galaxies: active – galaxies: formation – galaxies: high-redshift – galaxies: starburst – radio lines: galaxies

**Online-only material:** color figures

## 1. INTRODUCTION

Over the past decade, great progress has been made in understanding the conditions for star formation in gas-rich galaxies out to the highest redshifts. Molecular gas, the prospective fuel for star formation, is now detected in more than 70 galaxies at  $z > 1$ , allowing us to compare the properties of star-forming environments among different galaxy populations in the early universe (see Solomon & Vanden Bout 2005 for a review). These detections are almost exclusively being obtained in rotational transitions of CO, which (due to its relatively low critical density of  $n_{\text{crit}}(\text{H}_2) \simeq 300 \text{ cm}^{-3}$ ) is a good proxy for the total amount of molecular gas in a galaxy.

More focused studies of the *dense* molecular gas found in the star-forming cores of molecular clouds typically employ observations of high dipole moment, high critical density ( $n_{\text{crit}}(\text{H}_2) > 10^4 \text{ cm}^{-3}$ ) molecules such as HCN, HCO<sup>+</sup>, and HNC, both in nearby galaxies and out to high  $z$  (e.g., Gao & Solomon 2004; Riechers et al. 2006a, 2007a; Gao et al. 2007; Baan et al. 2008; Gracia-Carpio et al. 2008).

We here aim to study, for the first time, the dense, star-forming molecular gas *excitation* in a high- $z$  galaxy. Constraints on the excitation of gas at very high densities and the physical mecha-

nisms (collisions versus other channels) responsible are crucial to understand in more detail how excitation may influence scaling relations between the dense gas content and star formation rate of galaxies back to early cosmic times. To disentangle excitation effects from other phenomena (such as the chemical composition of the gas), it is crucial to target multiple diagnostic lines in a well-studied, key system. The target of this study is the extremely luminous  $z = 3.91$  quasar APM 08279+5255, which has been studied comprehensively in CO and other diagnostics (see, e.g., Weiß et al. 2007; Riechers et al. 2009 for details). In particular, it is one of only two high- $z$  galaxies in which multiple dense molecular gas tracers were detected to date (the other being the Cloverleaf quasar at  $z = 2.56$ ; Barvainis et al. 1997; Solomon et al. 2003; Wagg et al. 2005; Riechers et al. 2006a, 2007b; Garcia-Burillo et al. 2006; Guelin et al. 2007).

In this paper, we report the detection of HCN( $J = 6 \rightarrow 5$ ), HCO<sup>+</sup>( $J = 6 \rightarrow 5$ ), and HNC( $J = 6 \rightarrow 5$ ) emission in the quasar host galaxy of APM 08279+5255 ( $z = 3.91$ ), using the Combined Array for Research in Millimeter-wave Astronomy (CARMA). These observations represent the first extragalactic detections of such high- $J$  lines of the dense gas tracers HCN, HCO<sup>+</sup>, and HNC, and significantly constrain the physical properties of the dense gas in the star-forming regions of this distant galaxy. We use a concordance, flat  $\Lambda$ CDM cosmology

<sup>6</sup> Hubble Fellow.

throughout, with  $H_0 = 71 \text{ km s}^{-1} \text{ Mpc}^{-1}$ ,  $\Omega_M = 0.27$ , and  $\Omega_\Lambda = 0.73$  (Spergel et al. 2003, 2007).

## 2. OBSERVATIONS

We used CARMA to observe the HCN( $J = 6 \rightarrow 5$ ) ( $\nu_{\text{rest}} = 531.7164 \text{ GHz}$ ), HCO<sup>+</sup>( $J = 6 \rightarrow 5$ ) (535.0618 GHz), and HNC( $J = 6 \rightarrow 5$ ) (543.8974 GHz) transition lines ( $\sim 560 \mu\text{m}$ ) toward APM 08279+5255. At  $z = 3.911$ , these lines are redshifted to 108.270, 108.952, and 110.751 GHz ( $\sim 2.8 \text{ mm}$ ). The target was observed with 14 or 15 antennas (corresponding to 91 or 105 baselines per antenna configuration) for 14 tracks in 2008 March and June (setup 1; HCN/HCO<sup>+</sup>, observed simultaneously) and 23 tracks between 2009 February and July (setup 2; HNC), amounting to a total observing time of 148 hr. This results in 37 hr on source time for HCN/HCO<sup>+</sup> and 52 hr for HNC. All HCN/HCO<sup>+</sup> observations were carried out in D array (11–148 m baselines), while HNC observations were carried out in the C, D, and E arrays (6–185 m baselines after flagging). Observations before 2008 June were carried out with the previous generation 3 mm receivers, and observations after 2008 March were carried out with the new generation 3 mm receivers (which offer improved noise temperatures, tuning range, and stability).

Weather conditions scaled between acceptable and excellent for observations at 3 mm wavelengths. For the HCN/HCO<sup>+</sup> observations, typical median phase rms values were  $275 \mu\text{m}$  (normalized to a 100 m baseline, measured at  $45^\circ$  elevation), median optical depths were  $\tau_{230\text{GHz}} = 0.24$ , and median precipitable water vapor columns were 3.9 mm. For the HNC observations, typical median phase rms values were 300 (C array),<sup>7</sup> 235 (D array), and  $395 \mu\text{m}$  (E array), median optical depths were  $\tau_{230\text{GHz}} = 0.38$ , and median precipitable water vapor columns were 5.5 mm. The nearby source J0818+423 (distance to APM 08279+5255:  $10''.6$ ) was observed every 20 minutes for secondary amplitude and phase calibration. The strong calibrator sources J0423–013, J0927+390, 3C 111, 3C 84, and 3C 273 were observed at least once per track for bandpass and secondary flux calibration. Absolute fluxes were bootstrapped relative to Mars, Uranus, or 3C 84 (when no planet was available). Pointing was performed at least every 2–4 hr on nearby sources, using both radio and optical modes. The resulting total calibration is estimated to be accurate within  $\sim 15\%$  (see the Appendix).

The 3 mm receivers were tuned between the HCN and HCO<sup>+</sup> lines at 108.611 GHz (setup 1) and at the redshifted HNC frequency of 110.751 GHz (setup 2), both in the upper sideband (USB). The intermediate frequencies were chosen to be 1.79 GHz for the HCN/HCO<sup>+</sup> observations (optimized for the previous generation receivers) and 2.50 GHz for the HNC observations (optimized for the new generation receivers), centering the lower sidebands (LSBs) at 105.031 and 105.751 GHz. Three bands with 15 channels of 31.25 MHz ( $\sim 85 \text{ km s}^{-1}$ ) width each were centered on the tuning frequencies. The bands were overlapped by two channels to improve calibration of the correlated data set, leading to an effective bandwidth of 1281.25 MHz ( $\sim 3500 \text{ km s}^{-1}$ ) per sideband. This comfortably covers the HCN, HCO<sup>+</sup>, and HNC emission lines as well as the 2.8 mm (rest-frame  $560 \mu\text{m}$ ) continuum of the source. It also provides coverage of the redshifted HC<sub>3</sub>N  $J = 57 \rightarrow 56$ ,  $59 \rightarrow 58$ , and  $60 \rightarrow 59$  lines ( $\nu_{\text{rest}} = 518.1897$ ,  $536.3420$ , and  $545.4170 \text{ GHz}$ ;  $\nu_{\text{obs}} =$

105.516, 109.212, and 111.060 GHz), as well as the SiO( $J = 12 \rightarrow 11$ ) line ( $\nu_{\text{rest}} = 520.8782 \text{ GHz}$ ;  $\nu_{\text{obs}} = 106.064 \text{ GHz}$ ). In particular, HC<sub>3</sub>N( $J = 57 \rightarrow 56$ ) lies in a spectral range that is covered by both LSB frequency setups.

For data reduction and analysis, the MIRIAD package was used. The final plots were created with the GILDAS package. All data were imaged using “natural” weighting, resulting in synthesized clean beams of  $4''.5 \times 3''.6$  (HCN/HCO<sup>+</sup>) and  $5''.3 \times 4''.6$  (HNC;  $\sim 29$  and  $35 \text{ kpc}$  at  $z = 3.91$ ). The CO size of the source is  $< 0''.4$  (Riechers et al. 2009), i.e., it is unresolved at the resolution of our observations. The final rms values for the HCN/HCO<sup>+</sup> and HNC observations are 0.15 and 0.13 mJy beam<sup>-1</sup> over the full USB bandpass (1281.25 MHz), and 0.95 and 0.88 mJy beam<sup>-1</sup> per 31.25 MHz ( $\sim 85 \text{ km s}^{-1}$ ) channel. The rms noise in the LSB is by 3% (HCN/HCO<sup>+</sup>) and 15% (HNC) better compared to the USB due to atmospheric transmission.

## 3. RESULTS

### 3.1. Emission Lines of High-density Gas Tracers

We have detected emission from the  $J = 6 \rightarrow 5$  HCN, HCO<sup>+</sup>, and HNC emission lines toward the  $z = 3.91$  quasar APM 08279+5255. The left panel of Figure 1 shows the HCN and HCO<sup>+</sup> spectrum at  $86 \text{ km s}^{-1}$  (31.25 MHz) resolution. Both lines are detected simultaneously on top of strong 2.76 mm continuum emission. The middle panel of Figure 1 shows the HNC spectrum at similar ( $85 \text{ km s}^{-1}$ ; 31.25 MHz) resolution. The line is also detected on top of strong continuum emission at similar wavelength (2.71 mm). Figure 2 shows the HCN and HCO<sup>+</sup> velocity channel maps at the same velocity resolution and coverage as the spectrum in Figure 1. At an rms of  $0.95 \text{ mJy beam}^{-1}$ , APM 08279+5255 is detected at  $8\sigma$  and  $6\sigma$  significance in the peak channels of the HCN and HCO<sup>+</sup> lines. Both emission lines are detected over 10 channels on top of the continuum, showing a decline in strength toward the linewings, as expected. Also, marginal excess flux is detected at the peak position of the redshifted HC<sub>3</sub>N( $J = 59 \rightarrow 58$ ) line, which however is not formally detected. Figure 3 shows the HNC velocity channel maps at the same velocity resolution as the spectrum in Figure 1 (central 12 channels). At an rms of  $0.88 \text{ mJy beam}^{-1}$ , the source is detected at  $6\sigma$  significance in the peak channel of the HNC line, also showing a decline in flux toward the line wings.

From simultaneous Gaussian fitting to the profiles of the HCN( $J = 6 \rightarrow 5$ ) and HCO<sup>+</sup>( $J = 6 \rightarrow 5$ ) lines and the underlying continuum emission, we derive HCN and HCO<sup>+</sup> line peak flux densities of  $4.04 \pm 0.61$  and  $2.48 \pm 0.56 \text{ mJy}$  and FWHM velocities of  $385 \pm 36$  and  $385 \pm 60 \text{ km s}^{-1}$ , respectively (in good agreement with the  $400 \pm 40 \text{ km s}^{-1}$  FWHM of HCN  $J = 5 \rightarrow 4$ ; Weiß et al. 2007). This corresponds to integrated HCN and HCO<sup>+</sup> line fluxes of  $1.65 \pm 0.19$  and  $1.01 \pm 0.19 \text{ Jy km s}^{-1}$ . A simultaneous fit to the HNC( $J = 6 \rightarrow 5$ ) line and underlying continuum emission yields a HNC line peak flux density of  $1.57 \pm 0.51 \text{ mJy}$  and a line FWHM of  $520 \pm 160 \text{ km s}^{-1}$  (also consistent with the FWHM of HCN  $J = 5 \rightarrow 4$  within the errors). This corresponds to an integrated HNC line flux of  $0.86 \pm 0.24 \text{ Jy km s}^{-1}$ . From the line peak velocities, we derive formal line redshifts of  $z = 3.9126 \pm 0.0011$  for HCN/HCO<sup>+</sup> (simultaneous fit), and  $z = 3.9144 \pm 0.0011$  for HNC, which are consistent with those derived from other molecular emission lines within the errors (e.g., Riechers et al. 2006b; Weiß et al. 2007).

<sup>7</sup> Only one 3 hr track was observed in C array, and all baselines  $> 185 \text{ m}$  were discarded due to the relatively high phase noise.

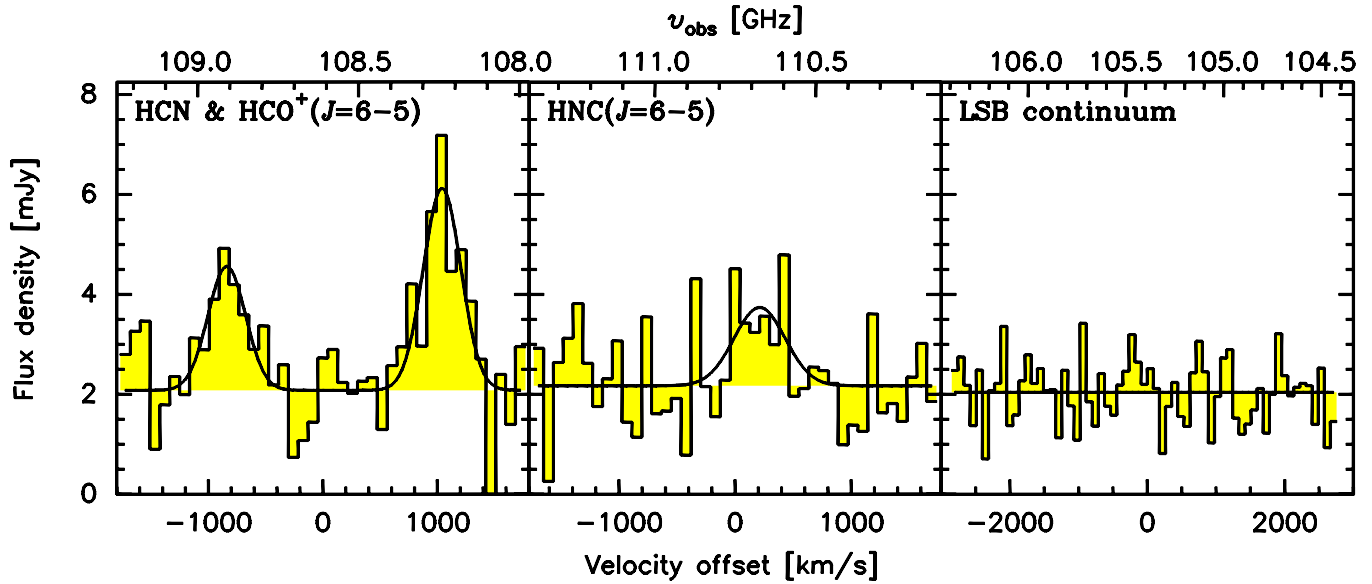


**Figure 1.** CARMA spectra of the HCN( $J = 6 \rightarrow 5$ ), HCO<sup>+</sup>( $J = 6 \rightarrow 5$ ) (left), HNC( $J = 6 \rightarrow 5$ ) (middle), and continuum emission at 2.76, 2.71, and 2.84 mm (left to right) toward APM 08279+5255 at a resolution of  $\sim 85 \text{ km s}^{-1}$  (31.25 MHz). The velocity scales are relative to the tuning frequencies of 108.611 GHz (left) and 110.751 GHz (middle) and the central frequency of both LSBs at 105.391 GHz (right). The rms per velocity bin are 0.95, 0.88, and  $\sim 0.65\text{--}0.92$  mJy (left to right). The solid curves show simultaneous Gaussian fits to the line and continuum emission where applicable.

(A color version of this figure is available in the online journal.)

**Table 1**

Measured Line Fluxes and Luminosities in APM 08279+5255

Line	$I$ (Jy km s <sup>-1</sup> )	$L'$ ( $10^{10} \mu_{\text{L}}^{-1} \text{ K km s}^{-1} \text{ pc}^2$ )
HCO <sup>+</sup> ( $J = 6 \rightarrow 5$ )	$1.01 \pm 0.19$	$3.0 \pm 0.6$
HCN( $J = 6 \rightarrow 5$ )	$1.65 \pm 0.19$	$4.9 \pm 0.6$
HNC( $J = 6 \rightarrow 5$ )	$0.86 \pm 0.24$	$2.4 \pm 0.7$
HC <sub>3</sub> N( $J = 57 \rightarrow 56$ ) <sup>a</sup>	<0.34	<1.0
HC <sub>3</sub> N( $J = 59 \rightarrow 58$ )	<0.52	<1.5
HC <sub>3</sub> N( $J = 60 \rightarrow 59$ )	<0.49	<1.4
SiO( $J = 12 \rightarrow 11$ )	<0.44	<1.3

**Notes.** All limits are  $3\sigma$ , extracted over a line width of  $400 \text{ km s}^{-1}$ . Luminosities are derived as described by Solomon et al. (1992):  $L'(\text{K km s}^{-1} \text{ pc}^2) = 3.25 \times 10^7 \times I \times v_{\text{obs}}^{-2} \times D_L^2 \times (1+z)^{-3}$ , where  $I$  is the velocity-integrated line flux in Jy km s<sup>-1</sup>,  $D_L$  is the luminosity distance in Mpc ( $z = 3.911$ ), and  $v_{\text{obs}}$  is the observed frequency in GHz. The given luminosities are not corrected for the lensing magnification factor of  $\mu_L = 4.2$  (Riechers et al. 2009).

<sup>a</sup> Covered by both frequency settings.

We also searched for HC<sub>3</sub>N  $J = 57 \rightarrow 56$ ,  $59 \rightarrow 58$ , and  $60 \rightarrow 59$ , as well as SiO( $J = 12 \rightarrow 11$ ) emission within the covered spectral range, including the LSBs (combined spectrum shown in the right panel of Figure 1). Marginal excess flux is seen close to the peak position of the redshifted HC<sub>3</sub>N( $J = 57 \rightarrow 56$ ) line in the overlap region of both LSB setups, which we however consider not detected in the following. We place  $3\sigma$  limits of 0.34, 0.52, 0.49, and 0.44 Jy km s<sup>-1</sup> on the integrated fluxes from these lines, extracted over a fixed velocity range of  $400 \text{ km s}^{-1}$  (see Table 1). We also attempted to stack all three HC<sub>3</sub>N lines, which results in no clear signal above the formal  $3\sigma$  limit of  $0.26 \text{ Jy km s}^{-1}$ . We however note that due to the uncertainties in extraction, this “stacked” limit has to be treated with caution.

### 3.2. Millimeter Continuum Emission

As mentioned above, we have detected  $\sim 2.8$  mm (rest-frame  $\sim 560 \mu\text{m}$ ) continuum emission toward the host galaxy of the

**Table 2**

Measured Continuum Fluxes in APM 08279+5255

$\nu_{\text{obs}}$ (GHz)	$\lambda_{\text{obs}}$ (mm)	$\lambda_{\text{rest}}$ ( $\mu\text{m}$ )	$S_{\nu}$ (mJy)
110.7	2.71	551	$2.17 \pm 0.19$
108.6	2.76	562	$2.08 \pm 0.22$
105.4 <sup>a</sup>	2.84	579	$2.04 \pm 0.08$
107.5 <sup>b</sup>	2.79	568	$2.08 \pm 0.07$

**Notes.**

<sup>a</sup> Combined LSB data from both setups.

<sup>b</sup> Averaged over all continuum data.

$z = 3.91$  quasar APM 08279+5255. Emission was detected at high signal-to-noise in each sideband of the two frequency setups. Thus, continuum fluxes were extracted by fitting a two-dimensional, elliptical Gaussian to the source in the  $u-v$  plane for each sideband and frequency setting, excluding ranges where line emission was detected. The individual values are listed in Table 2, and are fully consistent with the continuum fluxes obtained from the simultaneous line/continuum fits to the spectra as outlined above. A combination of all measurements yields an average continuum flux of  $2.08 \pm 0.07$  mJy at 2.79 mm, consistent with the spectral energy distribution (SED) of the source (Riechers et al. 2009).

### 3.3. Line Luminosities and Ratios

From the line intensities, we derive line luminosities and limits of  $L'_{\text{HCN}(6-5)} = (4.9 \pm 0.6)$ ,  $L'_{\text{HCO}^+(6-5)} = (3.0 \pm 0.6)$ ,  $L'_{\text{HNC}(6-5)} = (2.4 \pm 0.7)$ ,  $L'_{\text{HC}_3\text{N}(57-56)} < 1.0$ ,  $L'_{\text{HC}_3\text{N}(59-58)} < 1.5$ ,  $L'_{\text{HC}_3\text{N}(60-59)} < 1.4$ , and  $L'_{\text{SiO}(12-11)} < 1.3 \times 10^{10} \mu_{\text{L}}^{-1} \text{ K km s}^{-1} \text{ pc}^2$  (Table 1; not corrected for the lensing magnification factor of  $\mu_L = 4.2$ ; Riechers et al. 2009).

This corresponds to  $J = 6 \rightarrow 5$   $L'$  ratios of HCN/CO =  $0.46 \pm 0.07$ , HCO<sup>+</sup>/CO =  $0.28 \pm 0.06$ , and HNC/CO =  $0.23 \pm 0.07$  (relative to CO  $J = 1 \rightarrow 0$ ; Riechers et al. 2009). Such high line ratios would be unusual even in the respective ground-state ( $J =$

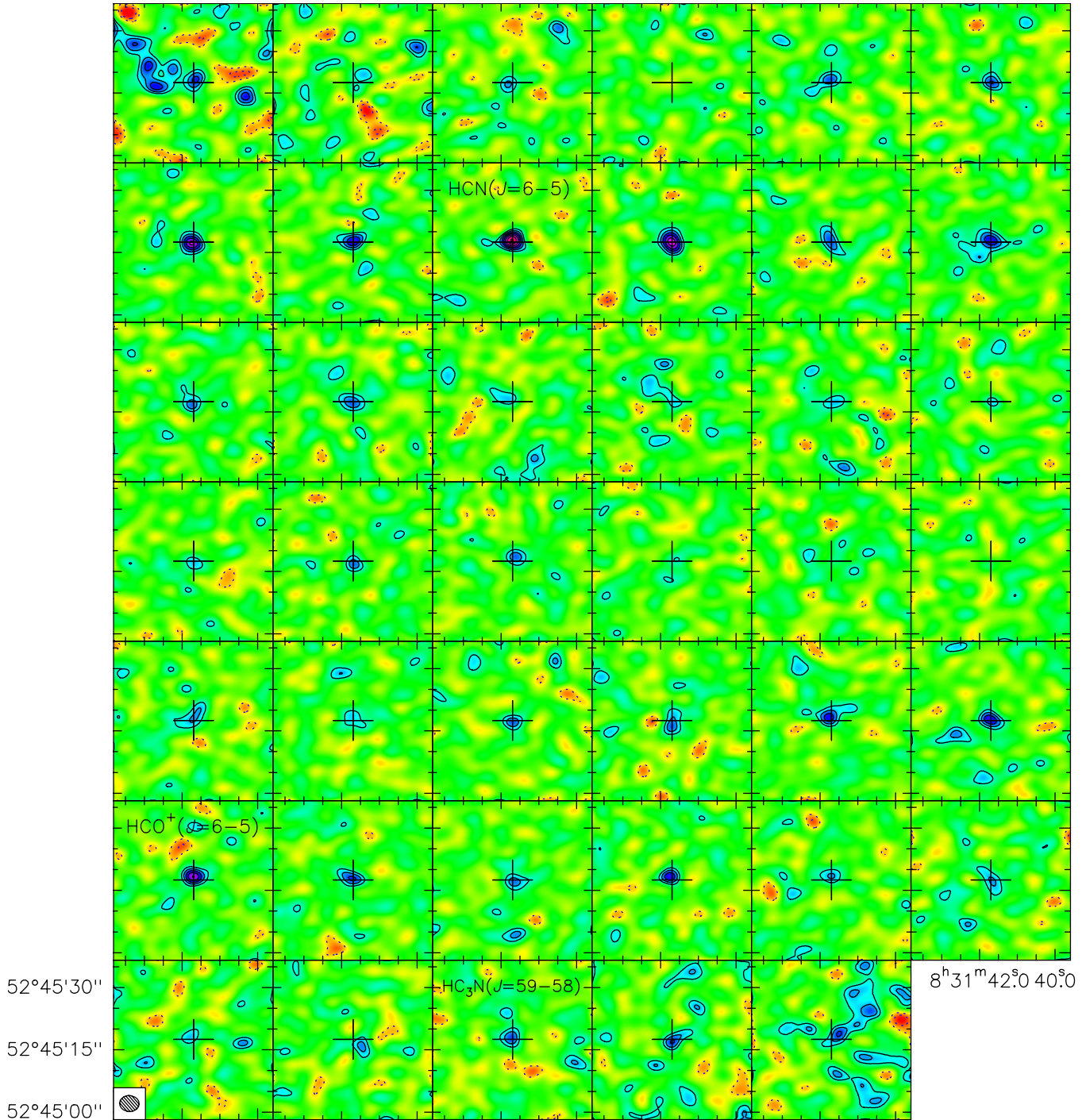


**Figure 2.** Channel maps of the data shown as a spectrum in Figure 1 (left) at the same velocity resolution. Frequencies increase with channel number from left to right, i.e., red to blue. The peak channels of the redshifted HCN, HCO<sup>+</sup>, and HC<sub>3</sub>N lines are indicated. Contours are shown at  $(-3, -2, 2, 3, 4, 5, 6, 7, 8) \sigma$  ( $1\sigma = 0.95 \text{ mJy beam}^{-1}$ ). The beam size ( $4''.5 \times 3''.6$ ) is shown in the bottom left corner. The cross indicates a position of  $08^{\text{h}}31^{\text{m}}41^{\text{s}}.70, +52^{\circ}45'17''.5$  between the CO lens images (Riechers et al. 2009).

(A color version of this figure is available in the online journal.)

$1 \rightarrow 0$ ) transitions, and indicate exceptional dense gas excitation conditions in this source.

We also find a HCN/HCO<sup>+</sup>  $J = 6 \rightarrow 5$   $L'$  ratio of  $1.7 \pm 0.4$ , which is higher than the HCN/HCO<sup>+</sup>  $J = 5 \rightarrow 4$   $L'$  ratio of  $1.0 \pm 0.2$  (Weiβ et al. 2007; Garcia-Burillo et al. 2006). Such a steeply rising HCN/HCO<sup>+</sup> line ratio with  $J$  is not expected, as the densities and temperatures to collisionally excite HCN and HCO<sup>+</sup> are similar. We note that the  $J = 5 \rightarrow 4$  lines were

not observed simultaneously, so the error bars of their ratio may be underestimated due to the uncertainties in their relative flux scales. In addition, the difference in line ratio with  $J$  may indicate that HC<sub>3</sub>N( $J = 49 \rightarrow 48$ ) line emission contributes significantly to the HCO<sup>+</sup>( $J = 5 \rightarrow 4$ ) flux reported by Garcia-Burillo et al., as these lines are blended. The HC<sub>3</sub>N limits derived above would be consistent with up to a 30%–40% contamination (extrapolated from these higher- $J$  transitions) of the HCO<sup>+</sup>( $J =$

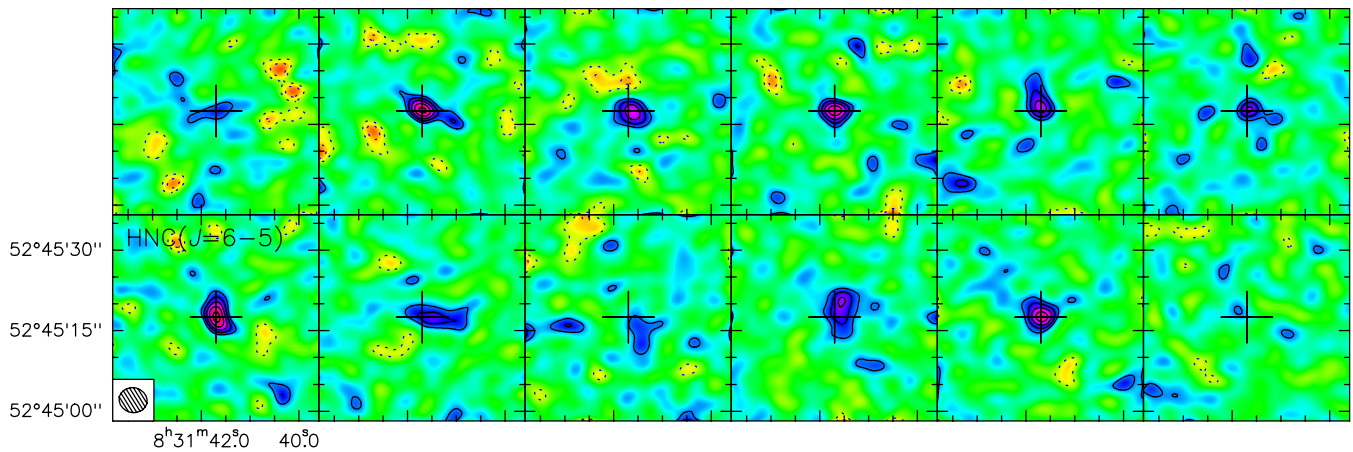


**Figure 3.** Channel maps of the central 12 channels of the data shown as a spectrum in Figure 1 (middle) at the same velocity resolution. Frequencies increase with channel number from left to right, i.e., red to blue. The peak channel of the redshifted HNC line is indicated. Contours are shown at  $(-3, -2, 2, 3, 4, 5, 6) \sigma$  ( $1\sigma = 0.88 \text{ mJy beam}^{-1}$ ). The beam size ( $5.3 \times 4.6''$ ) is shown in the bottom left corner. The cross indicates the same position as in Figure 2.

(A color version of this figure is available in the online journal.)

$5 \rightarrow 4$ ) flux. Note that such high  $\text{HC}_3\text{N}/\text{HCO}^+$  line ratios are actually observed in nearby infrared-luminous galaxies (albeit in lower- $J$  lines; e.g., Aalto et al. 2007a).

Furthermore, we find  $\text{HNC}(J = 6 \rightarrow 5)/\text{HCN}(J = 6 \rightarrow 5) = 0.50 \pm 0.15$  and  $\text{HNC}(J = 6 \rightarrow 5)/\text{HCO}^+(J = 6 \rightarrow 5) = 0.82 \pm 0.27$ . The  $\text{HNC}(J = 5 \rightarrow 4)$  line was observed toward APM 08279+5255, but it is strongly blended with  $\text{CN}(N = 4 \rightarrow 3)$  (Guelin et al. 2007). The single Gaussian fit by Guelin et al. to the blend of these lines can be translated to upper limits of  $\text{HNC}(J = 5 \rightarrow 4)/\text{HCN}(J = 5 \rightarrow 4) \leq 1.12$  and  $\text{HNC}(J = 5 \rightarrow 4)/\text{HCO}^+(J = 5 \rightarrow 4) \leq 1.15$ . Guelin et al. estimate that the CN line contributes  $\sim 1/3$  to the total flux they measure. Assuming their decomposition is correct, we find  $\text{HNC}(J = 5 \rightarrow 4)/\text{HCN}(J = 5 \rightarrow 4) = 0.64 \pm 0.32$  and  $\text{HNC}(J = 5 \rightarrow 4)/\text{HCO}^+(J = 5 \rightarrow 4) = 0.66 \pm 0.33$ . Given the similar excitation densities and temperatures of HNC compared to HCN and  $\text{HCO}^+$ , we assume that the  $J = 5 \rightarrow 4$  and  $6 \rightarrow 5$  line ratios should be comparable. This assumption is consistent with the observed  $\text{HNC}/\text{HCN}$  ratios if the CN contribution to the  $\text{HNC}(J = 5 \rightarrow 4)$   $L'$  is as suggested by Guelin et al. It also is consistent with the observed  $\text{HNC}/\text{HCO}^+$  ratios, in particular if the  $\text{HC}_3\text{N}$  contribution to  $\text{HCO}^+(J = 5 \rightarrow 4)$  is comparable to the CN contribution to  $\text{HNC}(J = 5 \rightarrow 4)$ . However, given the remaining uncertainties, observations of another CN transition would be desirable to test this scenario (see also discussion below).

Interestingly, we find a  $\text{HCN}(J = 6 \rightarrow 5)/\text{HCN}(J = 5 \rightarrow 4)$   $L'$  ratio of  $1.36 \pm 0.31$ . A ratio of greater than 1 is not expected for optically thick, collisionally excited emission that is thermalized or subthermal. However, such high  $L'$  ratios have also been found for HNC in nearby (ultra-) luminous infrared galaxies ((U)LIRGs), such as Arp 220 (albeit in lower- $J$  lines; Aalto et al. 2007b). Moreover, extreme gas densities of  $n(\text{H}_2) > 10^6 \text{ cm}^{-3}$  would be required to highly excite the  $J = 6 \rightarrow 5$  transitions of HCN, HNC, and  $\text{HCO}^+$  collisionally ( $n_{\text{crit}}(\text{H}_2) > 10^8 \text{ cm}^{-3}$ ).

#### 4. HCN LINE EXCITATION MODELING

To understand the unusual dense gas excitation in APM 08279+5255 in more detail, we have carried out large velocity gradient (LVG) models of the HCN line excitation (see Weiß et al. 2007 for initial study). Our models take both collisional and radiative excitation via infrared (IR) pumping into account, using the HCN collision rates from Schöier et al.

(2005), and including the first rovibrational bending mode at  $14.0 \mu\text{m}$  for pumping ( $v_2 = 1$ ; e.g., Thorwirth et al. 2003). We adopted a HCN abundance per velocity gradient of  $[\text{HCN}]/(dv/dr) = 1 \times 10^{-9} \text{ pc (km s}^{-1})^{-1}$  (Helfer & Blitz 1997; Wang et al. 2004). All parameters are required to also reproduce the CO excitation of the source (Weiß et al. 2007), assuming  $[\text{HCN}/\text{CO}] = 10^{-4}$ , and are required to be consistent with the dust SED (Weiß et al. 2007; Riechers et al. 2009). The best solutions were obtained for a spherical, single-component model with kinetic temperatures of  $T_{\text{kin}} = 220 \text{ K}$ , gas densities of  $n_{\text{gas}} = 10^{4.2} \text{ cm}^{-3}$ , an infrared radiation field temperature of  $T_{\text{IR}} (= T_{\text{dust}}) = T_{\text{kin}} = 220 \text{ K}$ , and infrared filling factors<sup>8</sup> of  $\text{IR}_{\text{ff}} = 0.3\text{--}0.7$  (Figure 4; where solutions with higher  $\text{IR}_{\text{ff}}$  prefer slightly lower  $T_{\text{kin}}$  to stay consistent with the observed size of the source in CO emission; Riechers et al. 2009).

Due to the high intensity of the IR-pumping field (as indicated by  $\text{IR}_{\text{ff}}$ ) in these models,  $\text{HCN}(J = 5 \rightarrow 4)$  and  $\text{HCN}(J = 6 \rightarrow 5)$  are only moderately optically thick (typical optical depths of  $\tau_{5-4} = 0.25$  and  $\tau_{6-5} = 0.4$ ), and the optical depth still rises with  $J$  between these lines. This implies that the excitation of HCN is not “super-thermal” (as in a “true” population inversion between energy levels), but that the high HCN  $L'$  ratio is merely an optical depth effect. The HCN excitation is dominated by IR pumping for all models that fit the data. Interestingly, the models imply that the HCN emission cannot dominantly arise from a relatively cold, dense gas, and dust component (see Weiß et al. 2007 for multi-component models). This means that standard conversion factors  $\alpha_{\text{HCN}} = M_{\text{dense}}/L'_{\text{HCN}}$  from HCN line luminosity to dense gas mass (e.g., Gao & Solomon 2004) will substantially overpredict the dense molecular gas mass in this system. Also, the models do not require unusually high relative HCN abundances, contrary to previous suggestions based on a narrower exploration of the parameter space in excitation conditions (Garcia-Burillo et al. 2006).

#### 5. DISCUSSION

##### 5.1. $\text{HCO}^+$ and HNC Excitation

Due to the remaining uncertainties in the  $\text{HCO}^+(J = 5 \rightarrow 4)$  and  $\text{HNC}(J = 5 \rightarrow 4)$  line intensities (see discussion above), it

<sup>8</sup>  $\text{IR}_{\text{ff}}$  describes the solid angle fraction of the gas that is exposed to the IR field, which in turn is described by a greybody spectrum.

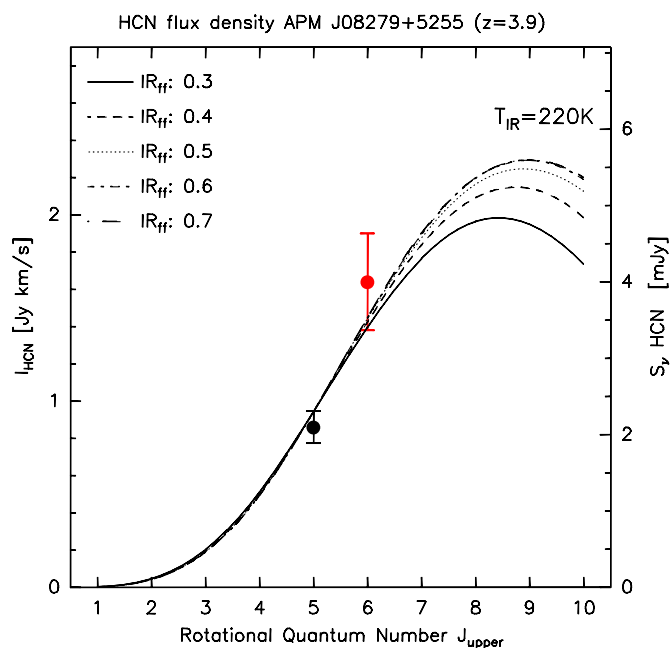


**Figure 4.** HCN excitation ladder (spectral line energy distribution; points) and LVG models (lines) for APM 08279+5255, accounting for both collisional and radiative excitation. The HCN( $J = 5 \rightarrow 4$ ) data point is from Weiß et al. (2007). The models give  $n_{\text{gas}} = 10^{4.2} \text{ cm}^{-3}$ ,  $T_{\text{kin}} = T_{\text{IR}} = 220 \text{ K}$ , and infrared field-filling factors of  $\text{IR}_{\text{ff}} = 0.3\text{--}0.7$  (shown in steps of 0.1).

(A color version of this figure is available in the online journal.)

is currently not possible to properly constrain similar models for the HCO<sup>+</sup> and HNC line excitation. However, due to similar rovibrational bending modes ( $\nu_2 = 1$  at 12.1 and 21.6  $\mu\text{m}$ ), it is likely that similar conclusions hold for the HCO<sup>+</sup> and HNC excitation. The bending modes of HCN, HCO<sup>+</sup>, and HNC all lie close to the peak of the dust SED of APM 08279+5255 (Weiß et al. 2007; Riechers et al. 2009), which would make such a scenario plausible. Also, the organic compound HC<sub>3</sub>N has several bending modes in this wavelength regime (e.g., Wyrowski et al. 1999), which would make a substantial HC<sub>3</sub>N( $J = 49 \rightarrow 48$ ) contribution to HCO<sup>+</sup>( $J = 5 \rightarrow 4$ ) plausible. Luminous, high- $J$  HC<sub>3</sub>N emission consistent with radiative excitation scenarios is observed in nearby galaxies like NGC 4418 (Aalto et al. 2007a). On the other hand, the lowest rovibrational transition of the diatomic molecule CN lies at 4.9  $\mu\text{m}$  (see also Guélin et al. 2007), which lies substantially beyond the peak of the SED. No strong 4.9  $\mu\text{m}$  (observed frame 24  $\mu\text{m}$ ) CN absorption is detected toward the bright mid-infrared continuum of APM 08279+5255 in deep *Spitzer Space Telescope* spectroscopy (D. Riechers et al. 2010, in preparation). Thus, IR pumping is likely substantially less effective for CN (relative to HCN, HCO<sup>+</sup>, and HNC), which may contrast<sup>9</sup> the relatively high CN( $N = 4 \rightarrow 3$ ) luminosity suggested by Guélin et al. (2007), depending on the actual CN abundance. However, luminous CN( $N = 3 \rightarrow 2$ ) emission was detected toward another distant lensed galaxy, the Cloverleaf quasar ( $z = 2.56$ ; Riechers et al. 2007b).

If CN and/or HC<sub>3</sub>N transitions close to those blended with HNC( $J = 5 \rightarrow 4$ ) and HCO<sup>+</sup>( $J = 5 \rightarrow 4$ ) are found to be much fainter than expected based on the  $L'$  estimates by Guélin et al.

<sup>9</sup> The high CO excitation in APM 08279+5255 can be explained by collisional excitation alone (Weiß et al. 2007); however, due to its higher critical density, collisional excitation of CN is substantially less effective than for CO.

(CN) and above (HC<sub>3</sub>N), a more complex scenario would be required to explain the different HCN, HCO<sup>+</sup>, and HNC line ratios in the  $J = 5 \rightarrow 4$  and  $6 \rightarrow 5$  transitions. In this case, it will become necessary to investigate the different efficiency with which the IR radiation field excites their bending modes in more detail, which may lead to high but different excitation for the rotational ladders of these molecules.

## 5.2. HNC/HCN Ratio

Recent studies of HCN and HNC emission in nearby infrared-luminous galaxies have revealed sources with high HNC/HCN ratios and high HNC excitation. Two scenarios were brought forward to explain these high ratios: IR pumping and/or increased abundances of HNC in the presence of X-ray-dominated regions (XDRs, often found in regions impacted by emission from active galactic nuclei; Aalto et al. 2007b). On the one hand, we find that HCN( $J = 6 \rightarrow 5$ )/HCO<sup>+</sup>( $J = 6 \rightarrow 5$ )  $> 1$ , which is the opposite to what is expected in the XDR scenario (Aalto et al. 2007b). However, we note that our LVG models show that the HCN( $J = 6 \rightarrow 5$ ) line (and thus, likely also the HNC  $J = 6 \rightarrow 5$  line) is only moderately optically thick, abundance effects thus cannot be ruled out. On the other hand, the HNC( $J = 6 \rightarrow 5$ )/HCN( $J = 6 \rightarrow 5$ ) ratio of  $0.50 \pm 0.15$  in APM 08279+5255 also fits well into the IR-pumping scenario: in nearby infrared-luminous galaxies, the gas is warm enough to efficiently pump HNC (through the 21.6  $\mu\text{m}$  bending mode with an energy level of  $h\nu/k = 669 \text{ K}$  and Einstein A coefficient of  $A_{\text{IR}} = 5.2 \text{ s}^{-1}$ ), but not HCN (through the 14.0  $\mu\text{m}$  bending mode  $h\nu/k = 1027 \text{ K}$  and  $A_{\text{IR}} = 1.7 \text{ s}^{-1}$ ; Aalto et al. 2007b), leading to a high HNC/HCN  $L'$  ratio in high- $J$  transitions. In APM 08279+5255, the dust and gas are warm enough to also efficiently pump HCN at high rates, so the line ratio depends mostly on the fraction of the HNC or HCN-emitting gas that is exposed to the IR radiation field and optical depth effects (given that the fraction of  $L'$  in the  $J = 6 \rightarrow 5$  transitions due to collisional excitation is likely small). This allows for a broad range of HNC/HCN ratios, and thus is consistent with the comparatively low  $J = 6 \rightarrow 5$  ratio, especially in combination with the high excitation of both molecular line spectral energy distributions (SLEDs). Similar arguments can be made for the relative strength of HCO<sup>+</sup>, which has its fundamental 12.1  $\mu\text{m}$  bending mode at slightly higher energy than HCN.

## 5.3. Detectability of Mid-IR Pumping Lines

Given the SED and brightness of the high- $J$  rotational lines of HCN, HNC, and HCO<sup>+</sup>, pumping by mid-IR rovibrational transitions appears plausible. As the abundance of these molecules is high enough to yield bright rotational lines in emission, the question arises whether or not the pumping transitions themselves may be detectable (which would place better constraints on the abundance of these molecules). The 14.0  $\mu\text{m}$  HCN feature was detected in absorption in nearby (U)LIRGs (Lahuis et al. 2007). Indeed, sources such as Arp 220 or NGC 4418 show deep absorption features (10%–30% of the continuum flux), indicating high HCN abundances, and evidence for pumping of the rotational HCN lines. The  $\nu_2 = 1$  lines of HCO<sup>+</sup>, HCN, and HNC are at rest-frame 12.1, 14.0, and 21.6  $\mu\text{m}$ , i.e., observed frame 59.4, 68.8, and 106.1  $\mu\text{m}$ , which is within the wavelength range of the Photodetector Array Camera and Spectrometer (PACS) on board the *Herschel Space Observatory* (e.g., Poglitsch et al. 2010). APM 08279+5255 has continuum fluxes of  $511 \pm 51$  and  $951 \pm 228 \text{ mJy}$  at 60 and 100  $\mu\text{m}$  (Irwin et al. 1998). Thus,

absorption features that have a depth of 10% of the continuum flux would be detectable within a few hours with *Herschel*.

## 6. CONCLUSIONS

Based on CARMA observations of HCN, HNC, and  $\text{HCO}^+$  ( $J=6\rightarrow 5$ ) toward the  $z=3.91$  quasar APM 08279+5255, evidence is consolidating that the dense, star-forming molecular gas in this source is substantially enhanced in brightness by IR pumping (on top of gravitational magnification of the source).<sup>10</sup> The unusual, hundreds of parsec scale, warm gas, and dust in this source appears to harbor a strong IR-radiation field that efficiently pumps the high- $J$  transitions of HCN, HNC, and  $\text{HCO}^+$  at rates well beyond those achieved by collisional excitation alone. At least in the case of HCN, this leads to moderately optically thick emission, which appears as “super-thermal” between  $J=5\rightarrow 4$  and  $6\rightarrow 5$  (due to a combination of high excitation and rising optical depth). These findings are consistent with the picture that the bulk of the gas and dust in this source is situated in a compact, nuclear starburst, where both the highly active galactic nucleus and star formation contribute to the heating.

Even though APM 08279+5255 is known to be an extreme system, radiative excitation of dense molecular gas tracers may also play a significant role in other high redshift galaxies, as it does in nearby infrared-luminous galaxies (e.g., Aalto et al. 2007b). This issue becomes increasingly important for the interpretation of observations of higher- $J$  ( $J > 2$ ) transitions of dense gas tracers such as HCN,  $\text{HCO}^+$ , and HNC, which are redshifted into the millimeter observing windows at high  $z$ , and thus will be primarily targeted toward galaxies in the early universe by future facilities such as the Atacama Large Millimeter/Submillimeter Array (ALMA).

We thank Christian Henkel for the original version of the LVG code. D.R. acknowledges support from from NASA through Hubble Fellowship grant HST-HF-51235.01 awarded by the Space Telescope Science Institute, which is operated by the Association of Universities for Research in Astronomy, Inc., for NASA, under contract NAS 5-26555. Support for CARMA construction was derived from the G. and B. Moore Foundation, the K. T. and E. L. Norris Foundation, the Associates of the California Institute of Technology, the states of California, Illinois, and Maryland, and the NSF. Ongoing CARMA development and operations are supported by the NSF under a cooperative agreement, and by the CARMA partner universities.

## APPENDIX

### FLUX CALIBRATION

The observations presented here were taken over the course of four (HCN &  $\text{HCO}^+$ )/six (HNC) months. It thus is necessary to correct the flux scale of individual tracks for the intrinsic variability of the phase calibrator. Given the relatively large number of tracks (14/23), this leads to a substantially improved flux calibration relative to the sparsely sampled, internal look-up table of MIRIAD.

Figure 5 shows the variability of J0818+423, the phase calibrator, bootstrapped relative to Mars, Uranus, and 3C84 (top panel), measured over the first band in the LSB at

<sup>10</sup> IR pumping may also explain the unusual excitation of low-ionization rest-frame ultraviolet absorption lines in proximate absorbers along selected sight lines toward the active galactic nucleus (which may arise from diffuse gas in the galaxy; Srianand & Petitjean 2000).

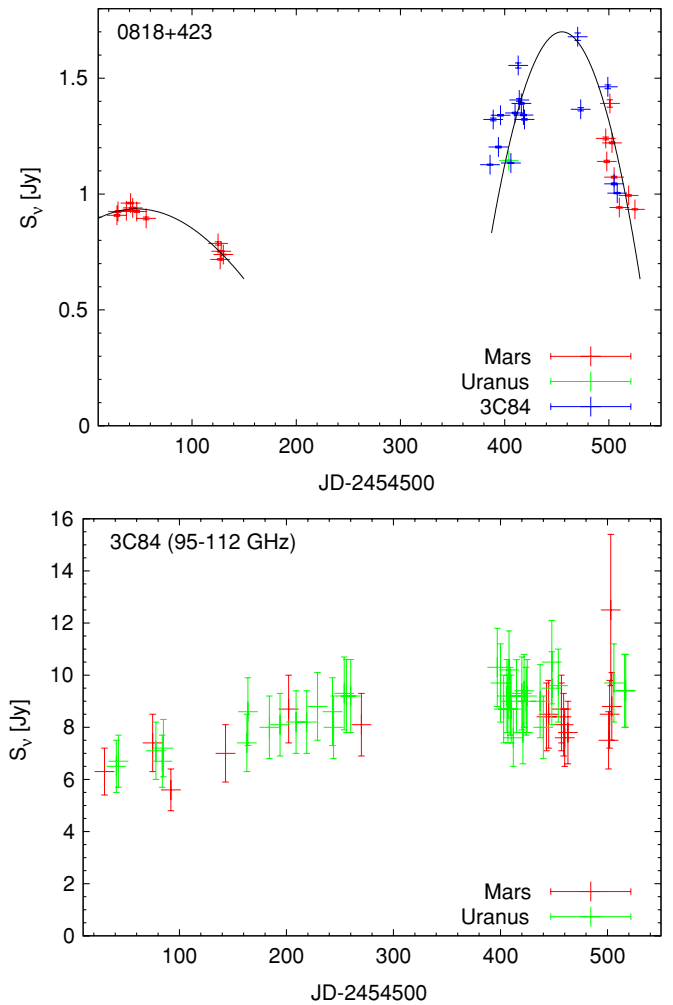


**Figure 5.** Millimeter variability of the phase calibrator J0818+423. Top: measured  $\sim 105$  GHz flux for the tracks in this project where a primary calibrator was observed, bootstrapped relative to the flux calibrators indicated in the bottom right corner. Error bars indicate the variance of individual measurements within a track. The black line indicates a fit to the data. Bottom: measured 95–112 GHz fluxes of 3C84 over the same time range (CARMA archive; S. Schnee 2009, private communication), bootstrapped relative to the flux calibrators indicated in the bottom right corner. Error bars include the absolute calibration uncertainty. This comparison shows that the variability among tracks bootstrapped relative to 3C84 is not due to intrinsic short-term variability of 3C84 itself.

(A color version of this figure is available in the online journal.)

$\sim 104.6/105.3$  GHz. For illustration, a fit to the data is shown. Fluxes for tracks that were observed without a primary calibrator were estimated based on a weighted average of those of tracks that are adjacent in time. As 3C84 is a millimeter-variable source itself,<sup>11</sup> the bottom panel shows its variability over the same time range in which this project was observed. Within the calibration errors, the phase calibrator shows a clear excess variability over that of 3C84 in the 2009 measurements (data points at  $(\text{JD}-2,454,500) > 332$ ). Also, the scatter of values in the 2009 measurements bootstrapped relative to the Mars planetary model is substantially larger than that in 2008 (typically observed under comparable weather conditions). Together with the fact that the fluxes bootstrapped relative to 3C84 agree well with those bootstrapped relative to planet models, this suggests that J0818+423 shows significant intrinsic flux variations over the observed time range. Thus, we obtain the best calibration by

<sup>11</sup> See, e.g., SMA data archive; <http://sma1.sma.hawaii.edu/callist/callist.html>.

using and interpolating the individually bootstrapped fluxes for each track, rather than using an averaged value for J0818+423. We conservatively estimate that this flux calibration leads to an overall accuracy of  $\sim 15\%$ .

## REFERENCES

- Aalto, S., Monje, R., & Martín, S. 2007a, *A&A*, 475, 479  
Aalto, S., Spaans, M., Wiedner, M. C., & Hüttemeister, S. 2007b, *A&A*, 464, 193  
Baan, W. A., Henkel, C., Loenen, A. F., Baudry, A., & Wiklind, T. 2008, *A&A*, 477, 747  
Barvainis, R., Maloney, P., Antonucci, R., & Alloin, D. 1997, *ApJ*, 484, 695  
Gao, Y., Carilli, C. L., Solomon, P. M., & Vanden Bout, P. A. 2007, *ApJ*, 660, L93  
Gao, Y., & Solomon, P. M. 2004, *ApJ*, 606, 271  
García-Burillo, S., et al. 2006, *ApJ*, 645, L17  
Graciá-Carpio, J., et al. 2008, *A&A*, 479, 703  
Guélin, M., et al. 2007, *A&A*, 462, L45  
Helfer, T., & Blitz, L. 1997, *ApJ*, 478, 233  
Irwin, M. J., et al. 1998, *ApJ*, 505, 529  
Lahuis, F., et al. 2007, *ApJ*, 659, 296  
Poglitsch, A., et al. 2010, *A&A*, 518, L2  
Riechers, D. A., Walter, F., Carilli, C. L., & Bertoldi, F. 2007a, *ApJ*, 671, L13  
Riechers, D. A., Walter, F., Carilli, C. L., & Lewis, G. F. 2009, *ApJ*, 690, 463  
Riechers, D. A., et al. 2006a, *ApJ*, 645, L13  
Riechers, D. A., et al. 2006b, *ApJ*, 650, 604  
Riechers, D. A., et al. 2007b, *ApJ*, 666, 778  
Schöier, F. L., van der Tak, F. F. S., van Dishoeck, E. F., & Black, J. H. 2005, *A&A*, 432, 369  
Solomon, P., Vanden Bout, P., Carilli, C., & Guélin, M. 2003, *Nature*, 426, 636  
Solomon, P. M., Radford, S. J. E., & Downes, D. 1992, *Nature*, 356, 318  
Solomon, P. M., & Vanden Bout, P. A. 2005, *ARA&A*, 43, 677  
Spergel, D. N., et al. 2003, *ApJS*, 148, 175  
Spergel, D. N., et al. 2007, *ApJS*, 170, 377  
Srianand, R., & Petitjean, P. 2000, *A&A*, 357, 414  
Thorwirth, S., Wyrowski, F., Schilke, P., Menten, K. M., Brünken, S., Müller, H. S. P., & Winnewisser, G. 2003, *ApJ*, 586, 338  
Wagg, J., Wilner, D. J., Neri, R., Downes, D., & Wiklind, T. 2005, *ApJ*, 634, L13  
Wang, M., et al. 2004, *A&A*, 422, 883  
Weiß, A., et al. 2007, *A&A*, 467, 955  
Wyrowski, F., Schilke, P., & Walmsley, C. M. 1999, *A&A*, 341, 882